

LA-UR-16-25356 (Accepted Manuscript)

Embedded fiber Bragg grating pressure measurement during thermal ignition of a high explosive

Rodriguez, George
Smilowitz, Laura Beth
Henson, Bryan Fayne

Provided by the author(s) and the Los Alamos National Laboratory (2017-01-11).

To be published in: Applied Physics Letters

DOI to publisher's version: 10.1063/1.4965842

Permalink to record: <http://permalink.lanl.gov/object/view?what=info:lanl-repo/lareport/LA-UR-16-25356>

Disclaimer:

Approved for public release. Los Alamos National Laboratory, an affirmative action/equal opportunity employer, is operated by the Los Alamos National Security, LLC for the National Nuclear Security Administration of the U.S. Department of Energy under contract DE-AC52-06NA25396. Los Alamos National Laboratory strongly supports academic freedom and a researcher's right to publish; as an institution, however, the Laboratory does not endorse the viewpoint of a publication or guarantee its technical correctness.

Embedded Fiber Bragg Grating Pressure Measurement during Thermal Ignition of a High Explosive

G. Rodriguez,^{1, a)} L. Smilowitz,² and B.F. Henson²

¹⁾Los Alamos National Laboratory, MPA-CINT K771, Los Alamos, New Mexico 87545 USA

²⁾Los Alamos National Laboratory, C-PCS J567, Los Alamos, New Mexico 87545 USA

(Dated: 28 October 2016)

A high-speed fiber Bragg grating based pressure-only measurement is reported for the high explosive PBXN-9 under thermal initiation conditions. During exothermic thermal runaway, an explosion rise time of 500 μ sec reaching a peak pressure of 660 MPa is measured. The approach offers a direct measure pressure diagnostic useful for quantifying reaction violence for high explosive chemistry.

PACS numbers: 06.60.Jn, 07.60.Vg, 47.40.Rs, 47.80.Fg

Keywords: fiber Bragg grating, high pressure sensor, high explosives, thermal ignition

Characterization of a high explosive response to thermal stimuli is important to understanding the violence in thermal explosions.^{1,2} To the extent that experimental observables such as density, temperature, pressure, and material flow, can be reliably monitored and recorded, approaches that yield this information greatly aid predictive models of reactive violence in strong exothermic reacting explosives. HMX (octahydro-1,3,5,7-tetranitro-1,3,5,7-tetrazocine) based plastic bonded explosives (PBXs) can vary in their burn propagation rate from 10's to 100's of meters per second and can undergo a deflagration to detonation transition.³ Radiography has been successfully used to determine differences in reaction rate violence in PBX based explosives.⁴ Yet, additional material state information is still needed, and approaches to measure dynamic temperature and pressure are scant.⁵⁻⁷ Direct pressure measurements in a burning high explosive are difficult to make because of the need for the sensor to survive elevated temperature, quasistatic volumetric flow due to the explosive material phase change, and high pressure. Additionally, the sensor must have high-speed (sub- μ sec) response without introducing an obtrusive perturbation to the experimental assembly. Recently, we reported on a successful embedded fiber approach that uses a single mode fiber Bragg grating to measure the response in thermal ignition experiments.⁸ The technique was shown to successfully measure strain and pressure under dynamic loading. Yet, from the pressure measurements reported⁸ of the HMX based plastic bonded explosive PBX-9501, it was not clear if the FBG temperature response was coincident and contributing to late time pressurization measurement since FBG sensors are known to have a coupled pressure and temperature response.⁹ In this paper, we show in the explosive PBXN-9, known to have nearly an order of magnitude slower burn rate than PBX 9501, that these (and previous) FBG pressure measurements are valid and not affected by the FBG thermal response

even in the slow burn limit of PBXN-9.

Approaches to decouple pressure (P) and temperature (T) have been published using highly birefringent polarization maintaining (PM) FBG sensors^{10,11} where tracking of the fast and slow axis of the PM-FBG reflection spectra allows for unambiguous determination of P and T independently. Simultaneous determination of pressure and temperature with a birefringent FBG is accomplished by solving the two variable (P, T) matrix equation. Beginning with the fractional Bragg grating wavelength ($\Delta\lambda_B$) shift response to pressure and temperature change (ΔT):

$$\frac{\Delta\lambda_B}{\lambda_B} = -\left(1 - \frac{n^2}{2}[p_{12} + B(p_{11} + p_{12})]\right)\left(\frac{1 - 2\nu}{E}\right)P + \left(\alpha + \frac{1}{n}\frac{dn}{dT}\right)\Delta T, \quad (1)$$

we identify the main parameters that determine FBG response to P and T loading. The fiber optical index is n , and the strain-optic photoelastic coefficients are the p_{ij} terms. B , $\nu=0.19$, and $E\approx 70$ GPa are the biaxiality strain ratio,¹² Poisson's ratio, and Young's modulus, respectively. The final two factors in front of the temperature change term are the thermal expansion coefficient (α), and the thermo-optic coefficient ($\frac{1}{n}\frac{dn}{dT}$) of the fiber index. Equation (1) must then be generalized for the birefringent response of a PM-FBG with a reflection spectrum that contains orthogonal ordinary (fast-axis, x) and extraordinary (slow-axis, y) polarization components that independently respond to the applied loading. The result is a 2×2 matrix equation that can be solved for P and T if the Bragg wavelength shift of both polarization components are measured:

$$\begin{bmatrix} \Delta\lambda_{Bf}/\lambda_B \\ \Delta\lambda_{Bs}/\lambda_B \end{bmatrix} = \begin{bmatrix} K_{Pf} & K_{Tf} \\ K_{Ps} & K_{Ts} \end{bmatrix} \begin{bmatrix} P \\ \Delta T \end{bmatrix}, \quad (2)$$

where, $K_{Pf,s}$ and $K_{Tf,s}$ are the collection of coefficients in front of the P and T terms of Eqn (1) for the fast-axis and slow-axis, respectively. In our measurements, we use 1-mm-long $\lambda_B=1555$ nm PM-FBGs manufactured by O/E Land, Inc. (La Salle, Quebec, Canada) on germanium doped, high birefringent (HiBi), bow-tie type,

^{a)}Electronic mail: rodrigeo@lanl.gov.

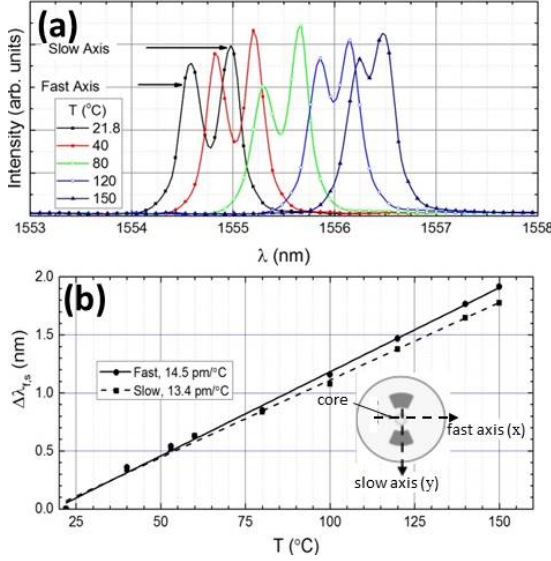


FIG. 1. A spectrometer measurement of the temperature response of a 1-mm-long HB1500P bow-tie PM-FBG immersed into a temperature controlled liquid mineral oil bath yields (a) the spectral shift and (b) slope fit to the peak shifts for the fast and slow axes of the PM-FBG sensor at $\lambda \approx 1555$ nm.

polarization maintaining polymide coated single mode HB1500P fused silica fiber from Fibercore, Ltd (Southampton, Hampshire, UK). The coefficients for temperature response are dominated by the thermo-optic response, $\frac{1}{n} \frac{dn}{dT} = 8.6 \times 10^{-6} \text{ } ^\circ\text{C}^{-1}$ compared to the thermal expansion coefficient, $\alpha = 5.5 \times 10^{-7} \text{ } ^\circ\text{C}^{-1}$.¹³ Differences in K_{Tf} versus K_{Ts} were directly measured by immersing the bow-tie PM-FBG in a temperature controlled mineral oil bath over a temperature range of 22 °C to 150 °C while the reflection spectrum was recorded with a spectrometer. Limitation to 150 °C in the temperature coefficient calibration test was limited by the boiling point of the mineral oil (160 °C). Figure 1(a) shows the reflection spectrum of the bow-tie PM-FBG with the fast and slow axis peaks well separated as the temperature is varied. Figure 1(b) plots the wavelength red shift of the peak(s) showing a linear shift in temperature, but with slightly different slopes for the fast (14.5 pm/°C) and slow (13.4 pm/°C) axes. Normalization of the fitted slopes to the average initial wavelength, $\lambda_B = 1555$ nm, yields the values of $K_{Tf} = 9.3 \times 10^{-6} \text{ } ^\circ\text{C}^{-1}$ and $K_{Ts} = 8.6 \times 10^{-6} \text{ } ^\circ\text{C}^{-1}$ for the two temperature coefficients in Eqn. 2. We note these temperature coefficients are consistent with the thermo-optic response coefficient, α , quoted earlier as the dominant temperature response mechanism in silica fiber.¹³ The pair of fractional Bragg wavelength strain coefficients $\Delta\lambda_{Bf}$ and $\Delta\lambda_{Bs}$ are determined by the appropriate set of strain coefficients responsible for the fast (x) and slow (y) response:¹²

$$\frac{\Delta\lambda_{Bf}}{\lambda_B} = \epsilon_z - \frac{n^2}{2} [p_{11}\epsilon_x + p_{12}(\epsilon_y + \epsilon_z)], \quad (3)$$

$$\frac{\Delta\lambda_{Bs}}{\lambda_B} = \epsilon_z - \frac{n^2}{2} [p_{11}\epsilon_y + p_{12}(\epsilon_x + \epsilon_z)], \quad (4)$$

where, the mean index of refraction, n , between the fast and slow axes is used. We note that if there is significant transverse strain along the components of the polarization axes, there is a peak separation in the Bragg strain shifted wavelength response that is proportional to the difference in transverse strains ϵ_x and ϵ_y :

$$\frac{\Delta\lambda_{Bf} - \Delta\lambda_{Bs}}{\lambda_B} = \frac{n^2}{2} (p_{12} - p_{11})(\epsilon_x - \epsilon_y). \quad (5)$$

However, because the pressure wave detected in our experiments is primarily longitudinal (axial) along the fiber's z-axis, and based on our measurement results presented here, we assert that $\epsilon_x = \epsilon_y$. This assertion postulates that no additional pressure dependent birefringence is induced into the fiber core, and as a consequence, the strain induced fast and slow axis fractional Bragg wavelength shifts are equal, *i.e.*, $(\Delta\lambda_{Bf}/\lambda_B) = (\Delta\lambda_{Bs}/\lambda_B) = [1 - (n^2/2)(p_{12} + B(p_{11} + p_{12}))]\epsilon_z$. After converting the axial strain (ϵ_z) to a pressure variable (P) using the relation: $\epsilon_z = (1 - 2\nu)P/E$, the pressure coefficients K_{Pf} and K_{Ps} of Equation (2) are realized and computed using values of photoelastic coefficients of $p_{11} = 0.121$ and $p_{12} = 0.27$, $E = 70$ GPa as Young's modulus, and a Poisson's ratio of $\nu = 0.19$.^{12,14} The mean refractive index of the fiber core is $n = 1.465$, and the intrinsic birefringence of the fiber is $\Delta n = 5.34 \times 10^{-4}$ ($n_f = 1.4647$ and $n_s = 1.4653$ are the indices of the fast and slow axes, respectively).¹⁵ A biaxiality ratio, $B = (\epsilon_x/\epsilon_z) = 0.88$, is chosen match the pressure response of bowtie HB1500P FBG to hydrostatic loading previously measured.¹⁶ Plugging in these values yields $K_{Pf} = K_{Ps} = -3.02 \times 10^{-6} \text{ MPa}^{-1}$, which is equivalent to a pressure induced wavelength shift of -4.7 pm/MPa at $\lambda_B = 1555$ nm. Therefore, the resultant 2×2 matrix equation describing the Bragg wavelength shift at $\lambda_B = 1555$ nm is:

$$\begin{bmatrix} \Delta\lambda_{Bf} \\ \Delta\lambda_{Bs} \end{bmatrix} = \begin{bmatrix} -4.7 & 14.5 \\ -4.7 & 13.4 \end{bmatrix} \begin{bmatrix} P \\ \Delta T \end{bmatrix}, \quad (6)$$

where, the coefficient units for pressure and temperature are, pm/MPa and pm/°C, respectively.

Experimental details of our FBG interrogation time-stretch spectroscopy system are described elsewhere.⁸ In Figure 2 we illustrate a modified version of our previous ultrafast FBG interrogator now for polarization encoded sensing. The salient differences between this system and our previous version is the use of PM fiber optics from the interrogating laser, to the PM-FBG, and through the first optical circulator. Broadband (1510 nm-1610 nm) modelocked 90-fs pulses from an Erbium fiber laser centered at 1560 nm with a 100 MHz repetition rate are spectrally filtered and polarization encoded before being launched into a single mode PM fiber. The laser linear polarization is state is rotated to 45 degrees to ensure that both orthogonal polarization states (fast and slow axes) of the FBG are interrogated. The laser linear polarization is state is rotated to 45 degrees to ensure that

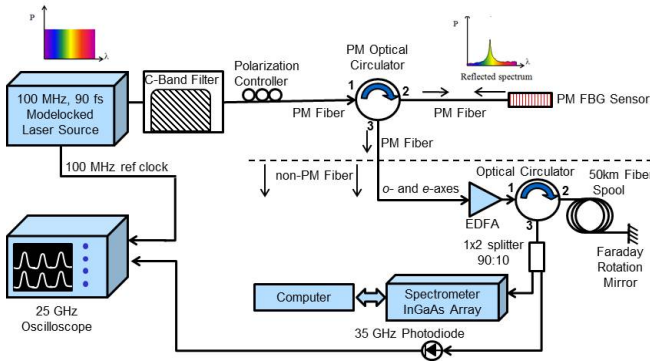


FIG. 2. Schematic illustrating the technique of FBG based time-stretch spectroscopy for simultaneous monitoring of o -axis and e -axis in a birefringent polarization maintaining Bragg grating (PM-FBG) sensor. The PM-FBG interrogation rate is 100 MHz, and the center wavelength of the PM-FBG is $\lambda \approx 1555$ nm.

both polarization states of the FBG are interrogated. After interrogating the PM-FBG polarization states, the output port of a 3-port PM optical circulator directs the pulses to the non-PM fiber portion of the interrogator system for optical amplification and chromatic dispersion (2×50 km) in Corning SMF28e fiber. The length of fiber used determines the amount of time stretching and wavelength resolution. The average dispersion constant for SMF28e fiber is 16.7 ps/nm/km. For 100 km of fiber, the effective spectral band between modelocked pulses (*i.e.*, 10 ns inter-pulse period) is 5.99 nm. After chromatic dispersion, time stretched pulse signals were amplified using a C-Band erbium doped fiber amplifier to boost the power losses introduced by the fiber spool to the few dBm level. A 35 GHz InGaAs photodetector converted the optical pulse train to electrical pulses for recording on a single channel of a 25 GHz, 100 GS/sec digitizing oscilloscope. The effective spectro-temporal resolution of the FBG time-stretch spectroscopy interrogator system is $\lambda_{res} = 0.024$ nm recorded every 10 ns in a 6 nm band between 1552 nm and 1558 nm.⁸ In addition to recording the optical time domain pulse train, a separate a non-time-resolving integrating InGaAs 512-element linear arrayed spectrometer (C-band: 1520 nm– 1570 nm, resolution: $\lambda_{res} = 0.1$ nm) is also used to record the PM-FBG reflection spectrum.

The PM-FBG sensor is inserted into an experimental metal cylinder package containing the loosely confined high explosive. A schematic and photograph of the experimental package assembly is shown in Fig. 3. Further details on the experimental package can be found in Refs.[8,17,18]. A pair of 12.5 mm diameter right cylinder pellets of the plastic bonded explosive PBXN-9 (high fraction HMX based explosive with soft binder) is used for these measurements. The pellets are stacked on top of each other so that midplane diagnostics (IR fiber pyrometry and thermocouples) can be placed in the center volume portion of the assembly as in Fig. 3(b). The high explosive (HE) pellets are housed in an end-capped aluminum sleeve. The HE is heated by a set of

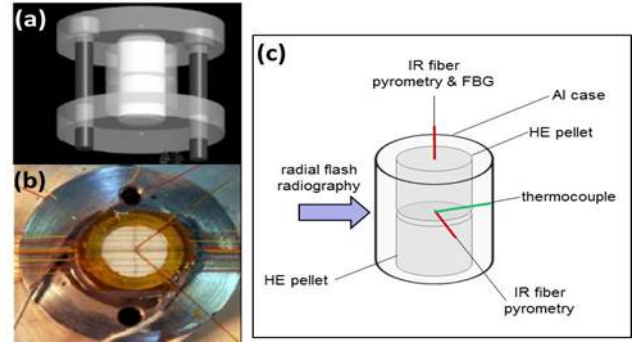


FIG. 3. (a) Schematics, and (b) photograph, showing the relative sizes and location of the aluminum case and encased high explosive pellets. In (b), the midplane section between two pellet halves is shown to expose the placement locations of the array of thermocouples and a pair of IR pyrometer optical fibers originating from the center. The illustration in (c) shows the relative placement locations of all the diagnostics: PM-FBG, thermocouples, pyrometer fibers, and x-ray flash radiography.

thin film resistive heaters attached to the case. Figure 3(c) illustrates the locations of the additional diagnostics. Thermocouples are used to independently monitor the temperature, and IR fiber pyrometry measures heat and light emission from the HE at the onset of ignition. Dynamic x-ray radiography^{17,18} is used to measure density changes and material flow during the final critical tens of microseconds leading to ignition and following the subsequent burn propagation. A single 1 -mm-long 1555 nm bowtie-type PM-FBG is embedded into the top of HE as illustrated in Fig. 3(c).

Experiments initially proceed by heating the sidewalls slowly over the period of 1.5 hours. Internal temperature measurements are continuously recorded using the signal from thermocouples with a computer controlled voltmeter, but since the FBG also responds to temperature, continuous recording of the FBG wavelength shift versus temperature is also done using the time integrating InGaAs array spectrometer. Thermally driven explosion experiments proceed by monitoring observables (usually internal HE temperature) over the course of the heating phase from which real time indicators in temperature are able to track subtle changes such as material phase change and HE chemistry induced self-heating effects. These indicators yield a measure of thermal decomposition before internal chemical reactive kinetics give way to a full self-sustaining explosion with ignition and burn propagation. Thermal decomposition occurs over time scales of hours. As exothermic chemistry begins, the material self-heats and the decomposition accelerates. This causes a thermal runaway which leads to the thermal explosion. Final steps in the development of a thermal explosion are observed via temperature and density to evolve on the time scale of seconds. Ignition then occurs and a switch in energy release to post-ignition time scales of microseconds is observed. Post-ignition burn propagation occurs for a duration of hundreds of microseconds and during this phase, extreme temperatures and pres-

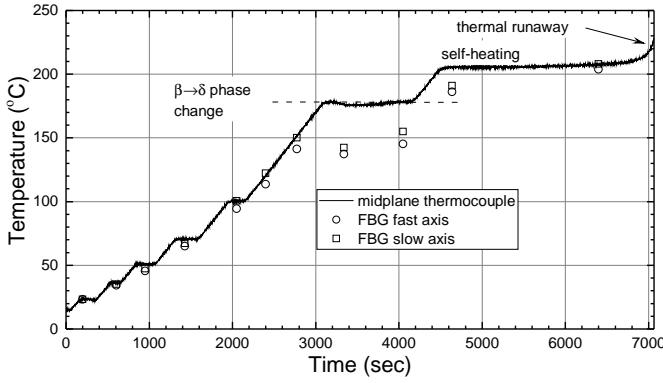


FIG. 4. A plot of the thermocouple and PM-FBG temperature history data for heated PBXN-9 is shown. The thermocouple data is the temperature measured at the midplane. The PM-FBG temperature data for the fast and slow axes are shown. The FBG does not track the thermocouple data during HE volume expansion and pressurization that occurs during the $\beta \rightarrow \delta$ phase change.

sures generated cause many other types of probes to fail. This is where the PM-FBG sensor interrogation speed becomes paramount. In Fig. 4 we plot the temperature time history during the thermal heating phase (*i.e.*, pre-ignition). The thermocouple data located at the midplane is shown, and the corresponding PM-FBG extracted temperature at several intermediate temperatures is overlaid as a symbol plot. The FBG temperature is measured by recording the spectrum with the InGaAs spectrometer and measuring the spectral red-shift of both, fast and slow, axes reflection spectra before converting the data using the calibration coefficients for spectral shift versus temperature. A temporary breakdown of the FBG temperature measurement occurs during the $\beta \rightarrow \delta$ phase transition. At the 175 °C point, the temperature is held to allow for material flow and rearrangement as the HMX undergoes a volumetric expansion due to the $\beta \rightarrow \delta$ crystalline phase transition. The FBG spectral response is affected and temporarily blue shifts during this period. After the phase transition, the FBG temperature measurement recovers, but at a much later time than the thermocouple. At the final hold temperature of 205 °C, reactive self-heating in the HE occurs in the final 1000 seconds before a full ignition. Post triggering of the oscilloscope is used to record the final ignition event and explosively driven pressure build up in the package using the FBG interrogation time-stretch spectroscopy system for the final 1 millisecond before the aluminum case containment fails and breaks up. Temperatures recorded during the initial stages of thermal runaway to ignition are in the ~ 230 °C range.

Plotted in Figure 5 are the PM-FBG measured results for a PBXN-9 experiment. Pressurization measured by the PM-FBG sensor begins as early as $t = -650$ μsec before the aluminum case disassembles at zero time. After pressurization, at $t = -88$ μsec , there is a rapid release of pressure (and subsequent ringing) that we hypothesize is due to the falling pressure in the blast wave

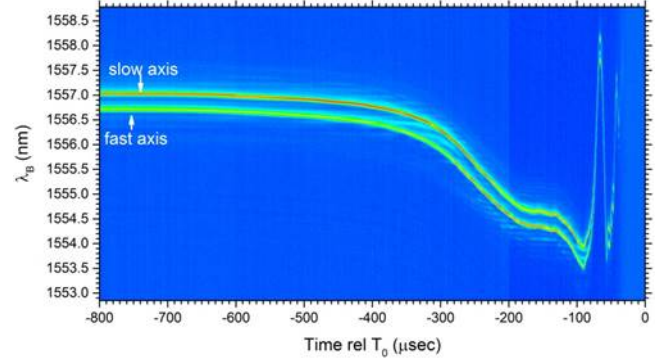


FIG. 5. Photodiode signal intensity map plot of the fast and slow axis Bragg wavelength shift (λ_B) versus time as measured by PM-FBG time-stretch spectroscopy interrogation system. T_0 is the post trigger zero time and marks the time point where aluminum case disassembly occurs and the experiment ends. The time axis, sampled at 100 MHz, yields a time resolution of 10 ns. The strong blueshift in the data indicates that pressure dominates the PM-FBG response, starting as early as -650 μsec .

that causes the spectrum to reverse direction (to longer wavelengths) upon pressure release. The pressure release coincides with the breakup of the Al case, endcap disassembly, and loss of confinement that is confirmed by the multi-frame flash x-ray images. After recording the peak pressure, the PM-FBG sensor survives the event to about $t = -40$ μsec before breakage. We also emphasize that the difference signal, $|\Delta\lambda_{Bf} - \Delta\lambda_{Bs}|$ is roughly constant, a good indication that transverse strains in the PM-FBG sensor are approximately equal (*i.e.*, $\epsilon_x \approx \epsilon_y$). After accounting for the offset in initial Bragg wavelength positions just before ignition, we plot the results in Figure 6 that shows the time resolved pressure profile. Using a pressure derived pressure coefficient of -4.7 pm/MPa, the pressure axis on Fig. 6(a) is shown on the right y-axis of the plot. The relatively slow build up pressure (100's of μsec) and measured peak pressure ($P_{max} = 660$ MPa) in PBXN-9 is in contrast to the results of PBX-9501 (few 10's of μsec , $P_{max} > 1500$ MPa) published in our previous paper⁸ and is a direct measure of the slower and lower explosive violence from PBXN-9 compared to PBX9501. The estimated uncertainty in the pressure measurement is $\pm 10\%$ based on the variation of the published values of the various constants used for determining the $K_{Pf,s}$ factors.^{11,15,19} This, however, is well within the $\pm 30\%$ shot-to-shot data scatter of the measured pressure in Ref.[8] caused by the stochastic nature of the initial ignition volume position relative to the location of the FBG sensor. Subtraction of the two curves in Fig. 6(a), yields the curve plotted in Fig. 6(b). Although one might expect that this could be the temperature-only component of the PM-FBG wavelength shift response (*i.e.*, $(\Delta\lambda_{Bf} - \Delta\lambda_{Bs}) = (14.5 \text{ pm}/^\circ\text{C} - 13.4 \text{ pm}/^\circ\text{C}) = 1.1 \text{ pm}/^\circ\text{C}$), we instead attribute the difference in fast and slow axis response to slight unequal response in the transverse strain components, ϵ_x and ϵ_y , and not a temperature dependence because the sign of the differ-

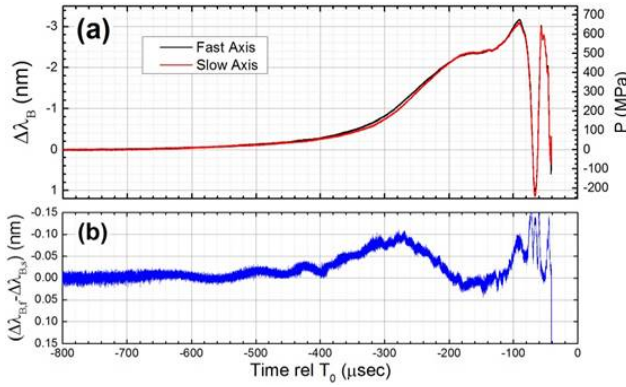


FIG. 6. Bragg wavelength shift (offset corrected) versus time is shown in (a). On the right ordinate axis we show the extracted pressure using the value of a pressure induced wavelength shift of -4.7 pm/MPa . In the lower panel plot (b), we plot the difference signal $(\Delta\lambda_{Bf} - \Delta\lambda_{Bs})$. This difference is attributed to a slight unequal response between the in-plane the transverse strain components, ϵ_x and ϵ_y , and is on the order of a few percent of the maximum Bragg wavelength shift measured.

ence is opposite to what would be expected for a temperature rise. Furthermore, the thermal conductivity and associated transport of fused silica is too slow to respond on the time scale of the observed difference between the fast and slow axes. An estimate of the thermal conduction time-constant required to heat a cylindrical-like fiber from the outer radius, $r_o = 62.5 \text{ } \mu\text{m}$, to center axis can be estimated as $\tau = r_o^2 / \alpha_T = 4.6 \text{ msec}$, where $\alpha_T = 8.5 \times 10^{-7} \text{ m}^2/\text{sec}$ is the thermal diffusivity for fused silica.²⁰ Thus, the fiber thermal response is too slow to measure temperature changes on the time scale of the pressurization dynamics during ignition.

In summary, we've demonstrated an approach to extracting high pressure-only measurements in a thermally ignited high explosive, PBXN-9. The observed peak pressure measured is 660 MPa rising slowly for approximately $550 \text{ } \mu\text{sec}$ post ignition. The approach establishes a baseline for understanding high explosive violence using an embedded FBG pressure measurement to quantify response. Future studies will include cross comparison to other explosives types, such as PBX-9501. Additional application to deflagrating processes is also envisioned.

This work was supported by the DOE/NNSA Science

Campaign 2, the Laboratory Directed Research and Development program, and the DOD/DOE Joint Munitions Program at Los Alamos National Laboratory under the auspices of the U.S. Department of Energy for Los Alamos National Security, LLC. Contract. No. DE-AC52-06NA25396.

- ¹B. Asay, editor, Shock Wave Science and Technology Reference Library Vol. 5: Non-Shock Initiation of Explosives (Springer-Verlag, Heidelberg, 2009).
- ²C.M. Tarver and S.K. Chidester, J. Pressure Vessel Technol. **127**(1), 39-48 (2005).
- ³A.P. Esposito, D.L. Farber, J.E. Reaugh, and J.M. Zaug, Propellants, Explos., Pyrotech. **28**, 83-88 (2003).
- ⁴L. Smilowitz, B.F. Henson, J.J. Romero, B.W. Asay, and the pRAD Collaboration, AIP Conf. Proc. **1195**, 436-439 (2009).
- ⁵F. Garcia, K.S. Vandersall, J.W. Forbes, C.M. Tarver, and D. Greenwood, AIP Conf. Proc. **845**, 1061-1064 (2006).
- ⁶P.A. Urtiew, J.W. Forbes, C.M. Tarver, F. Garcia, D.W. Greenwood, and K.S. Vandersall, Russian J. of Phys. Chem. B **1**(1), 46-51 (2007).
- ⁷E.A. Glascoe, H.K. Springer, J. Tringe, and J.L. Maienschein, AIP Conf. Proc. **1425**, 555-558 (2012).
- ⁸G. Rodriguez, M. Jaime, F. Balakirev, C. H. Mielke, A. Azad, B. Marshall, B.M. La Lone, B.F. Hensen, and L. Smilowitz, Opt. Express **23**(11), 0142189 (2015).
- ⁹S. Mihailov, Sensors 2012 **12**(2), 1898-1918 (2012).
- ¹⁰D. Wada, H. Murayama, H. Igawa, K. Kageyama, K. Uzawa, and K. Omichi, Smart Mater. Struct. **20**, 085028 (2011).
- ¹¹E. Chechura, C.-C. Ye, S.E. Staines, S.W. James, and R. P. Tatam, Smart Mater. Struct. **13**(4), 888-895 (2004).
- ¹²M. Lai, D. Karalekas, and J. Botsis, Sensors 2013 **13**(2), 2631-2644 (2013).
- ¹³A. Othonos, Rev. Sci. Instrum. **68**(12), 4309-4341 (1997).
- ¹⁴A. Bertgholds and R. Dandliker, J. Lightwave Technol. **6**(1), 17-20 (1988).
- ¹⁵A. Fernandez, H. Ottevaere, C. Van Ierschot, K. Oanajatov, F. Berghmans, and H. Thienpont, in Seventh Annual Proceedings of the 2002 Symposium of the IEEE/LEOS Benelux Chapter, Amsterdam, The Netherlands, 9 December 2002, edited by T. D. Visser, D. Lenstra, and H. F. Schouten pp. 139-144.
- ¹⁶E. Udd and W.B. Spillman, Jr, Fiber Optic Sensors (John Wiley & Sons Inc., Hoboken, 2011) pp. 440-447.
- ¹⁷L. Smilowitz, B.F. Henson, M. Holmes, A. Novak, D. Oschwald, P. Dolgonos, and B. Qualls, Rev. Sci. Instrum. **85**(11), 113904 (2014).
- ¹⁸L. Smilowitz, B. F. Henson, J. J. Romero, and D. Oschwald, Appl. Phys. Lett. **104**, 024107 (2014).
- ¹⁹E. Chechura, S.W. James, A. Johnstone, M. Lakrimi, F. Domp-tail, A. Twin, and R. P. Tata, Smart Mater. Struct. **20**(12), 125004 (2011).
- ²⁰A. F. Mills, Heat and Mass Transfer (Irwin, Chicago, 1995).